Research Article | Vol. 31, No. 14 / 3 Jul 2023 / Optics Express 23260

Optics EXPRESS

Thermo-optic VO_2-based silicon waveguide mid-infrared router with asymmetric activation thresholds and large bi-stability

MARK LUST,[1,*] ILYA VITEBSKIY,[2] IGOR ANISIMOV,[2] AND NIMA GHALICHECHIAN[3]

[1] *ElectroScience Lab, Department of Electrical and Computer Engineering, The Ohio State University, Columbus, OH, USA*
[2] *Sensors Directorate, Air Force Research Laboratory, Wright Patterson Air Force Base, Wright-Patterson, OH, USA*
[3] *mmWave Antennas and Arrays Lab, School of Electrical and Computer Engineering, Georgia Institute of Technology, Atlanta, GA, USA*
[*] *Lust.50@osu.edu*

Abstract: We report a novel four-port optical router that exploits non-linear properties of vanadium dioxide (VO_2) phase-change material to achieve asymmetrical power threshold response with power limiting capability. The scope of this study lies within the concept, modeling, and simulation of the device, with practical considerations in mind for future experimental devices. The waveguide structure, designed to operate at the wavelength of 5.0 µm, is composed of a silicon core with air and silicon dioxide forming the cladding layers. Two ring resonators are employed to couple two straight waveguides, thus four individual ports. One of the ring resonators has a 100-nm-thick VO_2 layer responsible for non-linear behavior of the device. The router achieves 56.5 and 64.5 dB of power limiting at the forward and reverse operating modes, respectively. Total transmission in the inactivated mode is 75%. Bi-stability and latching behavior are demonstrated and discussed.

1. Introduction

Asymmetry in optical devices is a phenomenon well-suited to the protection of delicate optical sensors that can be subject to high-power jamming signals or other unwanted input. As computation evolves from solid state transistors and diodes to lightwave circuits on chips, asymmetry can be used in integrated optical devices. Optical diodes have been previously demonstrated in free space with a blank vanadium dioxide (VO_2) thin film on a sapphire substrate and gold layer [1]. Previous studies explored dual-ring resonator devices where high-power signals activate VO_2 and allow signal passthrough [2]. There is also prior art on free-space phase change material (PCM) based optical metasurface [3] and multi-layer limiters and switching structures [4–7]; however, there is currently no published work on phase change material (PCM) based integrated optical limiters.

VO_2 is a PCM whose physical properties change with temperature, electric field, current, or strain. VO_2 undergoes a reversible change between monoclinic (dielectric) and tetragonal (metallic) phases around 68°C (341 K) [8], called the insulator-metal transition (IMT) or metal-insulator transition (MIT). For the purposes of this work, we use IMT to refer to the transition when heating, and MIT for the transition when cooling. This transition is sharp and nonlinear, making it an ideal sensing material in devices such as thermal imaging microbolometers [9]. It is particularly attractive for tunable and smart devices due to its low transition temperature and its ability to actuate from self-generated heat. VO_2 has a volatile phase transition, which adds to its appeal for smart devices because it requires no power to reset, unlike non-volatile PCMs such as

#493895 https://doi.org/10.1364/OE.493895
Journal © 2023 Received 25 Apr 2023; revised 14 Jun 2023; accepted 16 Jun 2023; published 27 Jun 2023

Optics EXPRESS

germanium telluride (GeTe) or its variant germanium antimony telluride (GST), which requires high melting temperatures above 891 K to return to its amorphous phase [10]. Additionally, VO_2 has a sub-picosecond intrinsic phase response time [11,12], meaning its switching speed depends only on the speed of the actuating stimulus. Finally, it is highly reliable, showing no degradation in operation after 100 million external heating and cooling cycles [13].

In the mid-infrared (mid-IR) bands, VO_2 is especially useful and efficient for smart and reactive devices. In the microwave domain, room-temperature VO_2 does not have sufficient conductivity and imaginary permittivity to effectively absorb power on its own [14,15]. It instead requires intimate contact with a lossy metal to be able to absorb incoming microwave radiation and subsequently transition. However, VO_2 at mid-IR and near-IR is slightly lossy at room temperature [16–18] and thus can act on its own as a self-heating material [1,7]. Once the activation temperature is reached, the VO_2 becomes extremely lossy, creating a positive feedback system that allows for self-activation and large bi-stability. This can be thought of as a quasi-latching behavior. It still requires power input to sustain the lossy state (unlike GeTe, which holds its altered phase), but the power requirement for maintaining the activated state is much lower than the one to initiate activation. The volatility of VO_2's transition is preferred over the fully latching behavior of GeTe in cases where PCM activation is needed many times in quick succession, as GeTe must be brought to its high melting temperature every time it switches to reset its phase. The choice of VO_2 for planar lightwave circuits is pragmatic not only for these properties and performance attributes, but also for realizing devices in nanofabrication. VO_2 deposition has been extensively investigated; it can be integrated with various substrates such as sapphire [8,17,19–25], quartz [17,26], and silicon [8,20,27–29]. Popular deposition techniques include sputtering [8,17,26,30] and pulsed laser deposition [21].

The remainder of the manuscript is organized as follows: Methods, Results and Discussion, and Conclusion. Methods details the design and simulation setup; Results and Discussion contains two subsections detailing the heating activation (insulator-metal transition, IMT switching behavior) and the cooling deactivation (metal-insulator transition, MIT switching behavior).

2. Methods

The goal of the router design concept is to combine asymmetric/diode-like behavior and routing ability in an on-chip planar lightwave circuit. The switching component is VO_2, which activates when the IR light causes it to heat up past its transition point of 68 °C. At low input power levels, light is passed through with minimal absorption, and at higher input power levels, light is blocked by the activated VO_2 and rerouted to an alternate output port. Once VO_2 is in its activated state, it is highly lossy, so the input power required to sustain beam routing decreases from the level required to activate. Conceptual schematics of each of these states are given in Fig. 1.

The proposed device acts as a power limiter for either direction of light propagation. The limiting threshold in our case is defined as the input power level triggering the dielectric-to-metal transition in VO_2. Due to the device asymmetry, the limiting threshold for the forward light propagation is different from that for the backward light propagation. The latter implies that if the input power lies between the two thresholds, the device will act as a magnet-free optical isolator (aka, optical diode), transmitting light only in one of the two opposite directions. This kind of "nonlinear" optical diode can be used for the broad-band protection of high-power sources from unwanted feedback. Another potential application is an asymmetric power switch or router. In any case, the difference between the forward and the backward limiting thresholds of the optimized device should be as large as possible.

The device in this work consists of two bus waveguides and two ring resonators. The device has four ports and is symmetric about the *xz*-plane as illustrated in Fig. 1. As such, the four directions of input are represented in two pairs of identical behaviors. This is for brevity and clarity of presentation; the two pairs of input directions are referred to hereafter as "forward" or

Optics EXPRESS

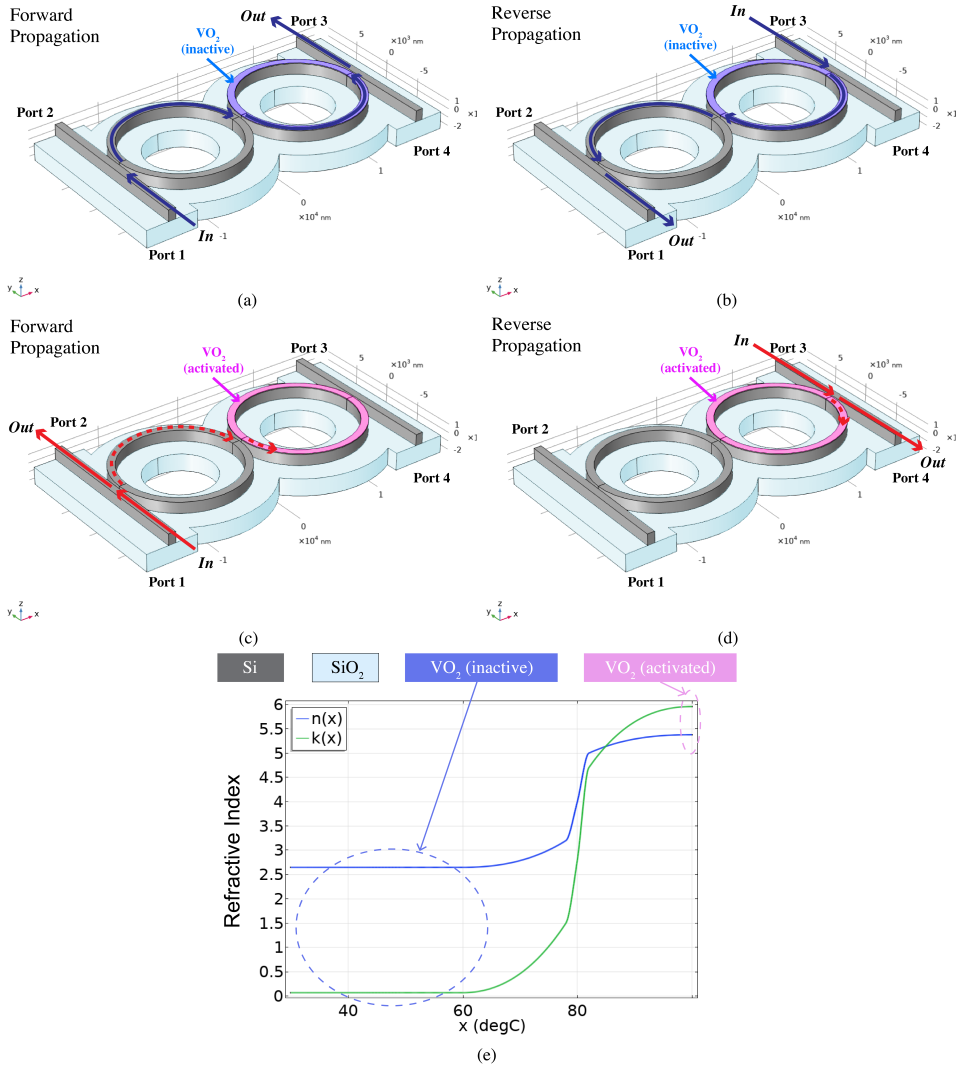

Fig. 1. Conceptual depictions of optical router operations, showing (a, c) forward propagation and (b, d) reverse propagation with VO_2 in (a, b) insulating state and (c, d) metallic state. Temperature-dependent real (n) and (k) refractive index of VO_2 is shown, measured at $\lambda = 5$ μm [16]. Insulator VO_2 has $n = 2.65$ and $k = 0.07$, and metallic VO_2 has $n = 5.38$ and $k = 5.96$.

Optics EXPRESS

"F" and "reverse" or "R". In each case, the light power initially routed to an output port is blocked and subsequently rerouted to another output port. In the forward case, F_{13} mode, the light enters via Port 1 and exits via Port 3; upon transition, the light to Port 3 is blocked and rerouted to Port 2. The latter is called F_{12}. In the reverse case, R_{31}, light enters via Port 3 and exits via Port 1; upon transition to the metallic (conductive) phase, the light to Port 1 is blocked and rerouted to Port 4 (R_{34} mode). The design goals of this device are to exhibit power limiting by > 40 dB with initial transmittance > 70%, while rerouting the blocked light at 50% transmittance.

The waveguide core is Si, with SiO_2 substrate and air as the upper cladding. One of the two ring resonators has a 100 nm layer of VO_2 on top. The other ring and both buses are Si only and are $w_{Si} = 850$ nm wide and $h_{Si} = 1300$ nm tall for a transverse magnetic (TM) fundamental mode. The Si + VO_2 ring has the same Si height but a smaller width of 800 nm such that the propagation constant, $\beta_g = 2.8959$, is consistent between both rings. Having matching propagation constants between the bus and ring waveguides was key to maximizing coupling between the buses and rings and between the two rings. These waveguide dimensions and the remaining device dimensions are given in Table 1. The key temperature-dependent material parameters for thermo-optic simulation of VO_2 are refractive index, thermal conductivity, and heat capacity. Below the IMT threshold (in dielectric phase), the refractive index is characterized as $n = 2.65$ and $k = 0.07$, and above the transition (in metallic phase), refractive index is $n = 5.38$ and $k = 5.96$. These refractive index values are based on interpolated measured data at λ=5 μm [16]; our interpolation is shown in Fig. 1. Thermal conductivity values are based on external measured data [26], and heat capacity is derived from measured electrical resistivity, published in previous work by our group [8,31]. Thermal conductivity ranges from 3.6 W/m•K at room temperature to 6 W/m•K above 349 K, and heat capacity ranges from 757 J/kg•K at room temperature to a peak value of 6053 J/kg•K at 347 K and reduces back to 958 J/kg•K at 363 K. Exact temperature-dependent property curves are available upon request.

Table 1. Device model parameters. Critical parameters are shown in bold

Description	Symbol	Value
Waveguide core width (Si)	$\boldsymbol{w_{Si}}$	**850 nm**
Bus length	l_{bus}	19.76 μm
Waveguide core width (Si + VO_2)	$\boldsymbol{w_{Si+VO2}}$	**800 nm**
Waveguide core height (Si)	$\boldsymbol{h_{Si}}$	**1300 nm**
VO_2 thickness	$\boldsymbol{h_{VO2}}$	**100 nm**
Circumference (electrical)	$\boldsymbol{m\pi}$	**20π**
Circumference (mechanical)	$\boldsymbol{C}$	**43.39 μm**
Ring-ring coupling distance	$\boldsymbol{d_{RR}}$	**250 nm**
Ring-bus coupling distance	$\boldsymbol{d_{RB}}$	**250 nm**
EWFD substrate height	$h_{sub,EWFD}$	2 μm
EWFD substrate/air width	$w_{sub,EWFD}$	5.95 μm
EWFD air height	$h_{air,EWFD}$	3.3 μm
HT substrate height x length x width	$h_{sub,HT}$ x $l_{sub,HT}$ x $w_{sub,HT}$	10 μm x 39.53 μm x 59.29 μm
HT air height x length x width	$h_{air,HT}$ x $l_{air,HT}$ x $w_{air,HT}$	15 μm x 39.53 μm x 59.29 μm

To build and simulate the model, we used COMSOL Multiphysics, with the Heat Transfer (HT) and Electromagnetic Waves Frequency Domain (EWFD) modules and the Electromagnetic Heating Multiphysics interface. These simulations are memory-, computation-, and time-intensive when performed on 3-D models with multiple beam paths and VO_2 non-linear phase change behavior. Single simulation runs frequently take 1-3 days to complete on a multi-processor server. Therefore, model adjustments are non-trivial and require careful conceptualizing between runs.

Optics EXPRESS

The device structure is seen in Fig. 2 and includes a set of domains containing only the waveguide core, substrate, and cladding for EM simulation and expanded domains of SiO_2 and air as bulk thermal material to ensure physical accuracy and restricting it to heat transfer only to reduce computation cost. Keeping computation cost down was key, as simultions involving the nonlinear self-activation of VO_2 can take several days to complete. In the EWFD parameters, numeric ports are used for all ports, and all ports have zero input power except the active port, which is set as port 1 for one case of input direction and port 3 for the other. The device is mirrored across the *zx*-plane; therefore, port 2 and 4 input cases are considered as exact, mirrored copies of the port 1 and port 3 inputs, respectively. To facilitate accurate representation of the guided mode, surrounding the core is 2 µm of SiO_2 substrate below, 3.3 µm of air above, and 2.55 µm air on either side. Perfect electric conductor (PEC) boundaries are used for the top and bottom faces of the air cladding and the substrate; these reduce computation cost without sacrificing accuracy, as all variation in field above and below the core is evanescent. The side walls of the EWFD domains are set as scattering boundaries so that the destructive interference at the coupling sides is accurate. The router is designed at mid-IR wavelengths 5.01–5.05 µm.

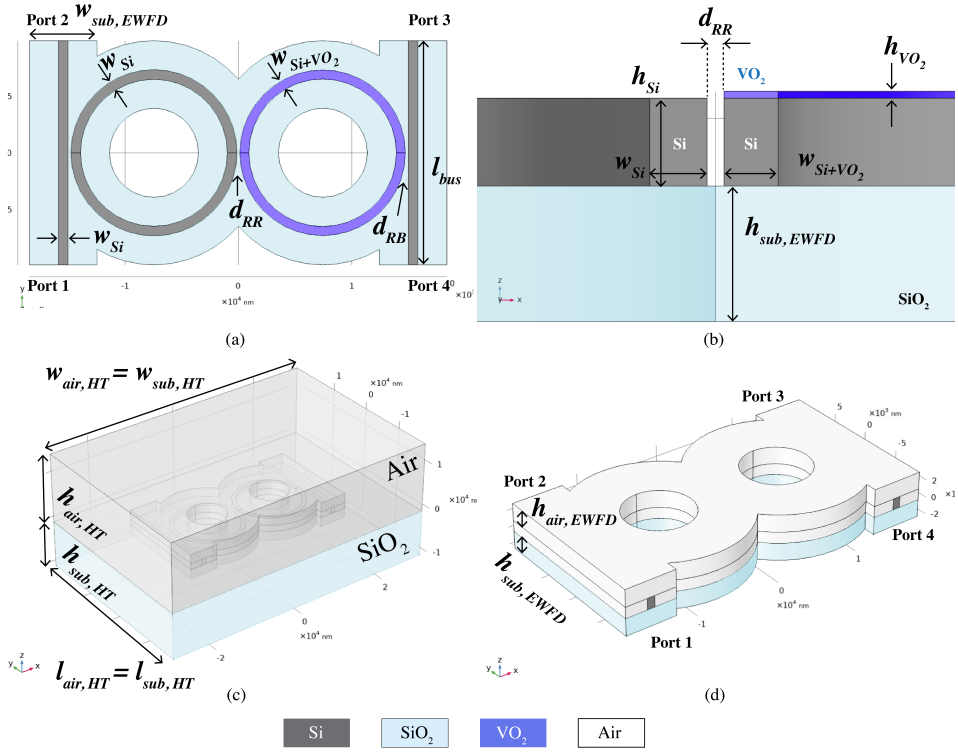

Fig. 2. Router geometry (a) top view, (b) cross-section of Si-only and Si + VO_2 waveguide (c) isometric view with expanded SiO_2 and air thermal domains, and (d) isometric view of strictly EM domains.

The coupling between the bus and ring waveguides involved considerations for fundamental propagation mode, device footprint, absorptive losses in VO_2, and maintaining realizable fabrication. Coupling is strengthened by increased surface area of the waveguide at the coupling interface, which can be accomplished via greater circumference to increase the length of the coupling interface or increasing the height of it by heightening the waveguides. Because VO_2 is slightly lossy at room temperature, it is preferable to reduce the length of beam propagation

Optics EXPRESS

through the Si + VO_2 waveguide and therefore reduce absorptive losses. For this reason, the overall performance was limited by the trade-off between increasing coupling and decreasing VO_2 absorption, both affected directly by the ring resonator circumference. To increase coupling without increasing the VO_2 absorption, we kept the circumference at 20π (43.49 μm) and designed using TM fundamental mode, rather than TE. Thus, we increased the height and consequently the surface area of the waveguides at the coupling interfaces. Coupling also increases with decreasing distance between the bus and ring and between the rings. With practical fabrication limitations in mind, we kept the distance at 250 nm.

For HT simulation, the boundaries of the outer airbox and substrate domain are set to room temperature or 293 K. This approach keeps model simplicity, giving reduced computation cost and time. We verified the technique in preliminary studies by increasing airbox and substrate domain size until no change was apparent in resultant behavior. Specifically, we examined the temperature profile in the VO_2 over time as we increased $h_{sub,HT}$, $l_{sub,HT}$, $w_{sub,HT}$, $h_{air,HT}$, $l_{air,HT}$, and $w_{air,HT}$. Once the temperature profiles were consistent from a smaller size of HT domain to larger, we were confident that the temperature is calculated correctly.

3. Results and discussion

The device is characterized in several modes of operation. To investigate the asymmetries in its behavior, we first established the room temperature resonant behavior, shown in Fig. 3. The router has an expanded 65% output port transmittance band of 5.010 μm to 5.048 owing to the dual-ring design. From here, we simulated the router with the power input to port 1 and port 3 to examine differences in switching behavior between the two cases of operation: source being from within the chip side (transmission) or source originating from without (receiving), or otherwise from different devices within the chip. The respective output ports at room temperature for port 1 and port 3 input are port 3 and port 1. Upon VO_2 IMT, the new output ports are port 2 and port 4, respectively. For all simulations, S_{41} and S_{23} are less than 2×10^{-5} as well as reflection. The device being symmetric about the zx-plane, the port 2 and port 4 input cases are mirrored exactly from port 1 and port 3 inputs and thus are fully represented in them and omitted for clarity of presentation.

The behavior described in this section is simulated at λ=5.015 μm, the first peak of output transmittance shown in Fig. 3. The H field is visualized in Fig. 4 for each input case at the initial time step (i.e., at room temperature) and when the VO_2 reaches and crosses through the IMT. The two input cases exhibit nearly identical initial port transmittance (T) and absorptance (A) (with S_{21} mapped to S_{43} and S_{31} mapped to S_{13}). At time $t = 0$, $S_{31} = S_{13} = 73.7\%$, $S_{21} = 1.5\%$, $S_{43} = 1.4\%$, and $A_{total,1} = 24.8\%$ and $A_{total,3} = 24.9\%$, with $T_{total,1} = 75.2\%$ and $T_{total,3} = 75.1\%$.

3.1. Heating and IMT switching behavior

After switching, the incoming light now sees different geometries, each having its path to the opposite bus severed. For port 1 input, the new output is port 2 with $S_{21} = 48.3\% = T_{total,1}$ and $A_{total,1} = 51.7\%$. The effective structure seen by the incoming wave can be considered as a lossy or leaky ring resonator. For port 3 input, the new output is port 4 with $S_{43} = 53.3\% = T_{total,3}$ and $A_{total,3} = 46.7\%$. The effective structure now seen by the incoming beam is a bus and coupler leading away and attenuating quickly. This behavior is presented graphically in Fig. 5 and depicted as well in decibel (dB) scale. Whereas the routing behavior is most easily described in percent values, the power limiting capabilities are best represented in dB; in the port 1 input case, power is limited by 56.5 dB, and in the port 3 input case, power is limited by 64.5 dB. The results shown are at the respective VO_2 activation power threshold for each input direction: 7.1 mW for port 1 input and 7.2 mW for port 3 input.

Furthermore, we see asymmetries in the temperature profile between the input cases. Visual observation of the temperature as seen in Fig. 6 shows similar profiles between the two cases in

Optics EXPRESS

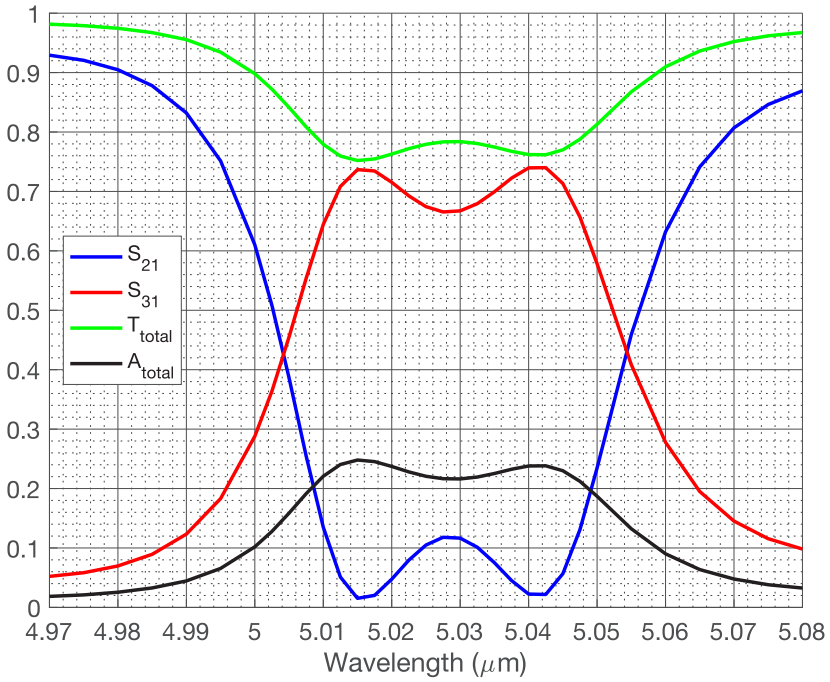

Fig. 3. Resonant port transmittance behavior of the router at room temperature.

the time steps leading up to the device switching, and then the highest temperature separately at the different sites of coupling. This follows as a matter of course, given that VO_2 becomes much lossier in the metallic state, thus the rapidly attenuating light will only produce heat where it is absorbed. Because of this increase in losses upon switching, there is positive feedback, giving a sharp increase in temperature by ~100 K, whereafter it levels off at ~430-440 K for the aforementioned threshold input power levels. Considering this positive feedback system, we examine the maximum temperature in the VO_2 volume; when any part of the VO_2 crosses the IMT, it causes the rest to follow suit.

Examining the maximum temperature profiles for the two input cases illustrated in Fig. 7, the most glaring distinction is that the IMT occurs in the port 1 input case at 7.1 mW but levels off in the port 3 input case. The IMT occurs at 7.2 mW in both cases but reaches different steady state temperatures of 443 K and 430 K for port 1 and port 3 inputs, respectively. Curiously, in the sub-threshold input power levels, the port 3 input reaches higher steady state temperatures per mW increase (5.74 K/mW) than port 1 (5.66 K/mW), a 1.4% asymmetry. The lower switching threshold for the port 1 input case is then informed by the difference in specific transient switching behavior—for port 1 input, the max temperature continues to increase in a linear fashion near the IMT temperature before fully switching, but the port 3 input exhibits a brief leveling-off before finally switching. Upon examination of the switching of the port 1 input case, one can see the dependence of switching time on input power. At the threshold (7.1 mW), the IMT takes 50 µs to complete, but an increase even as small as 0.1 mW shortens the switching time to 10 µs. This implies that higher levels of input power give shorter switching times valuable for power limiting application, but within the scope of this study, we are more interested in the behavior at threshold power.

Optics EXPRESS

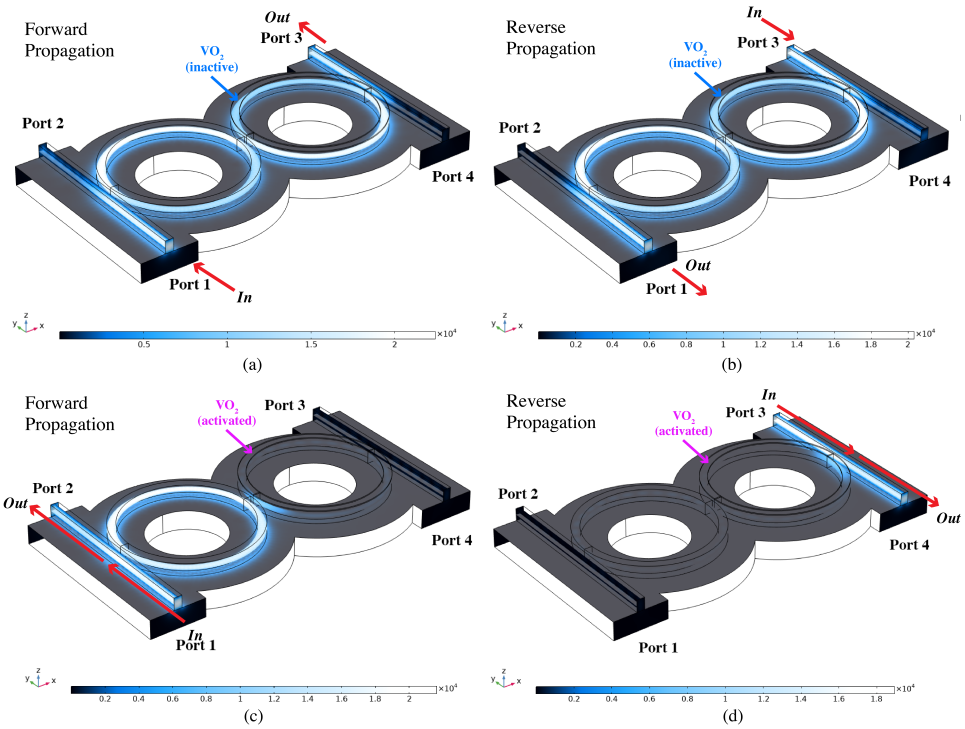

Fig. 4. Routing behavior of the device with (top row) VO_2 at room temperature (insulator state) and (bottom row) VO_2 after IMT (metallic state). The left column shows the forward device operation (port 1 as an input) or F_{13}, and F_{12} modes, respectively. The right column shows reversed operating modes of R_{31} and R_{34} (port 3 as an input). Color bar shows *H* field magnitude in A/m.

3.2. *Cooling and MIT switching behavior*

To study the bi-stability of the device, we began each cooling simulation with an initial step from the steady state of a 10 mW input power above the VO_2 IMT temperature, then used decreasing input power levels for a duration of 200 µs until the VO_2 fully deactivated (i.e., underwent the MIT). Additionally, the physical properties of VO_2 were shifted to be a function of (T–4 K) to account for the hysteresis in VO_2. We found that due to the positive feedback/self-heating property of VO_2, input power can be decreased down to 5 mW in each input case with no loss in rerouted power. This gives a 30% reduction in input power from the activation threshold to maintain light routing performance for port 1 input and a 31% reduction for port 3 input. Decreasing the input power to 4 mW yields only a small reduction in routing performance as the rerouted power decreases from $S_{21} = 48\%$ to $S_{21} = 46\%$ for port 1 input and from $S_{43} = 53\%$ to $S_{43} = 49\%$ for port 3 input. This above-MIT cooling behavior is seen in Fig. 8, along with dB scale and a more moderate degradation in routing performance at 3 mW input power: $S_{21} = 35\%$ and $S_{43} = 37\%$.

In each input case, the threshold for VO_2's MIT deactivation is 2.2 mW. This is a 69% reduction in input power to maintain VO_2's metallic state. The transition occurs at 68.9 µs for port 1, which is 5.6 µs earlier than port 3 input MIT, which occurs at 74.5 µs. This demonstrates that there is asymmetry in the deactivation of VO_2 as well as that which was demonstrated in the previous subsection for its activation. The sharp MIT takes 1.3 µs at deactivation threshold power for port

Optics EXPRESS

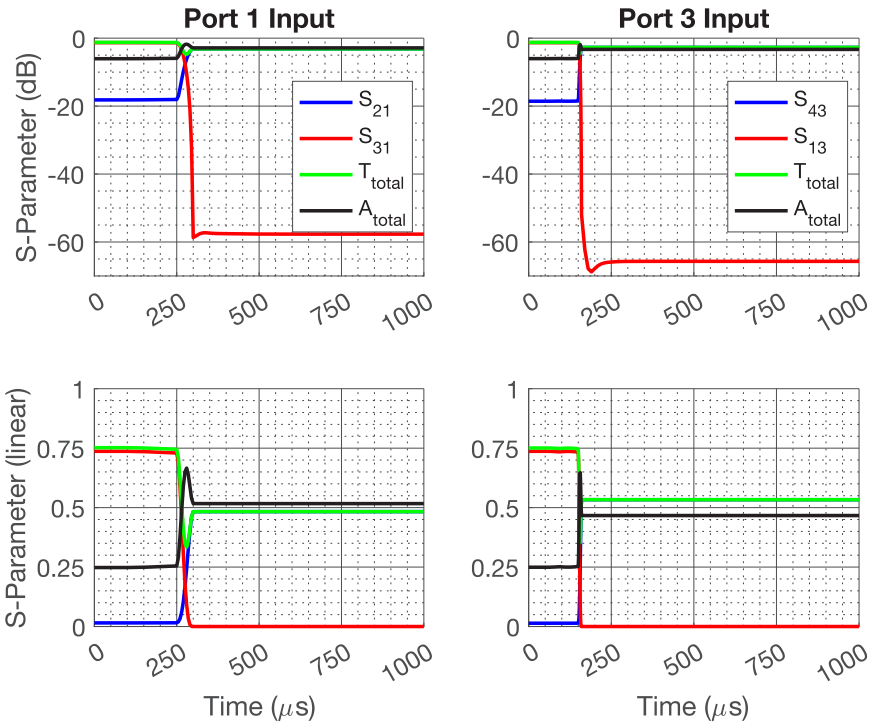

Fig. 5. Port transmittance behavior of the router through the IMT switching at VO_2 activation thresholds for port 1 input case (7.1 mW) and port 3 input case (7.2 mW).

1 input and 1.6 μs for port 3 input. The MIT switching port transmittance behavior is shown graphically in Fig. 9.

In the steady state maximum temperature profile, we find asymmetries as well. These differences are shown in Fig. 10. Firstly, the maximum temperature from the 10 mW initial condition is 500 K for port 1 input and 480 K for port 3 input. This is likely due to the heat in the port 1 input case being concentrated in an an area of the device that is more thermally isolated (i.e., less nearby thermal mass to act as heat sink) than in the port 3 case. Namely, for port 1 input, heat is concentrated near the ring-to-ring coupling site, and for port 3 input, the heat is concentrated near a ring-to-bus coupling site, where there is less distance through the substrate for heat to diffuse to nearby Si. From here, one can see that the steady state temperature is reached more quickly as power decreases, giving a nonlinear relationship between steady state temperature and input power when approaching the threshold.

Optics EXPRESS

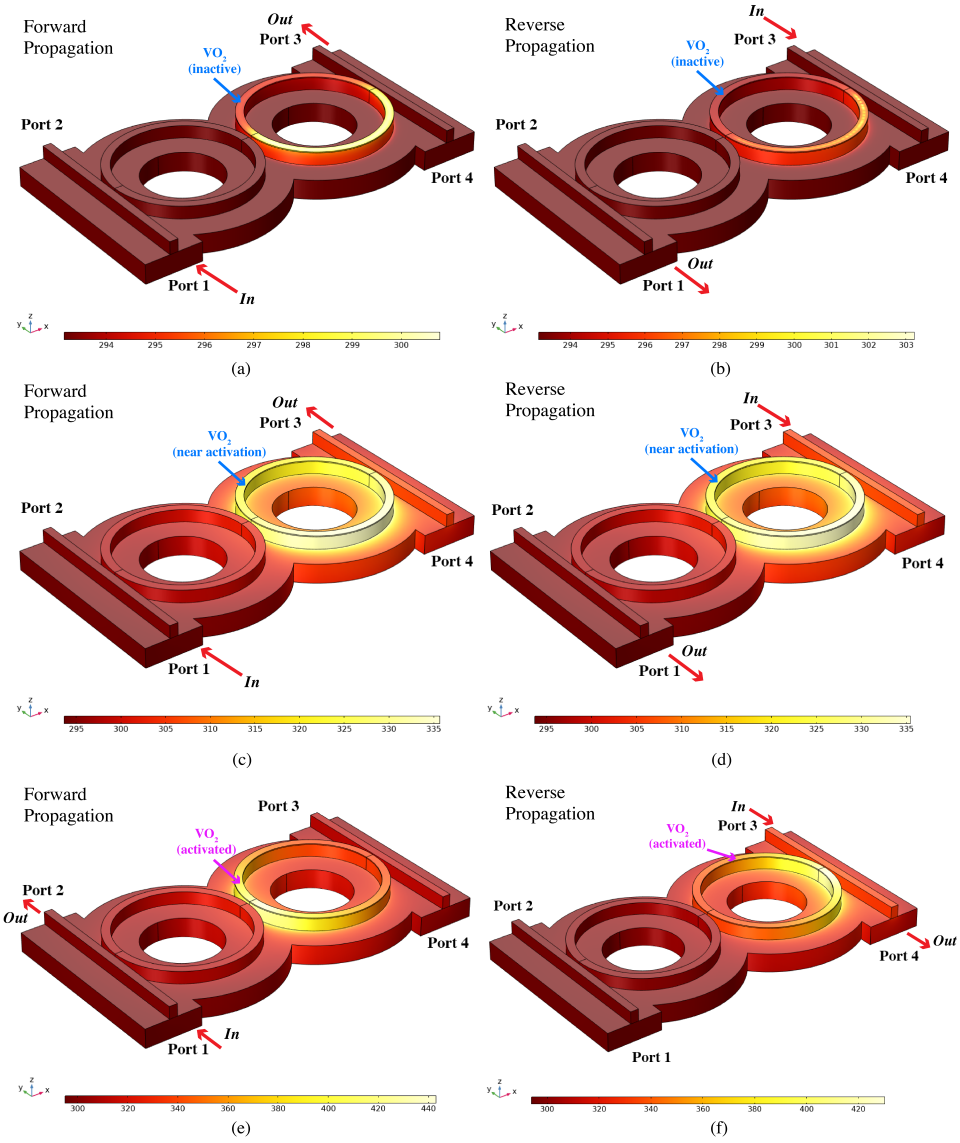

Fig. 6. Temperature profile of the device with (left column) port 1 input and (right column) port 3 input, at times t = 0.1 μs (a, b), 150 μs (c, d), and 1000 μs (e, f).

Optics EXPRESS

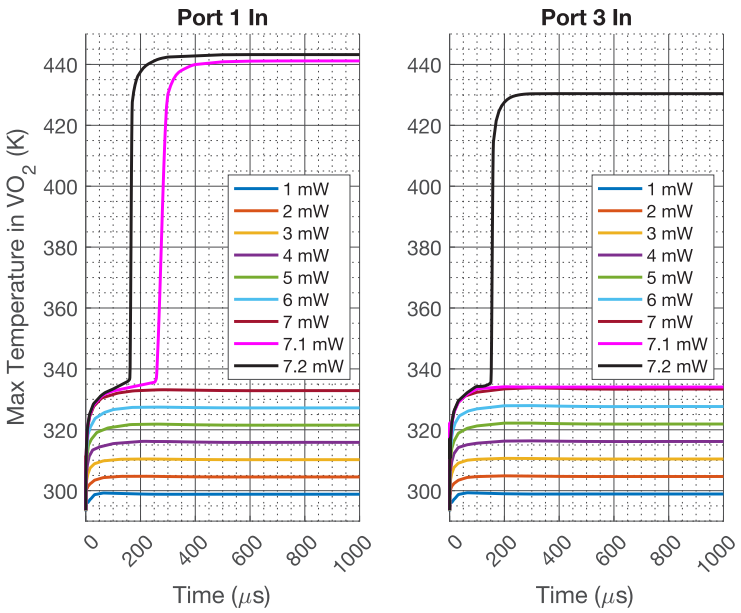

Fig. 7. Maximum temperature in VO_2 volume over the course of one millisecond to steady state, increasing input power approaching and including activation.

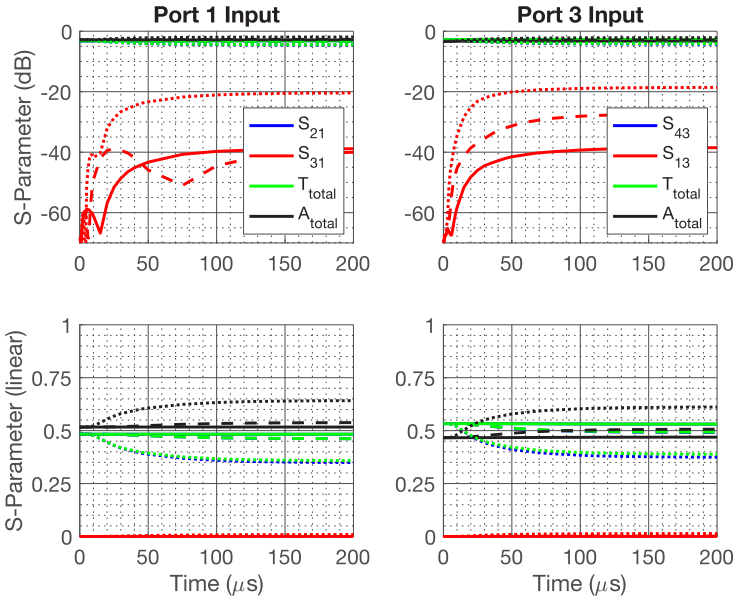

Fig. 8. Port transmittance behavior of the router when cooling but above MIT switching. Solid lines correspond to 5 mW input power, dashed lines to 4 mW, and dotted lines to 3 mW.

Optics EXPRESS

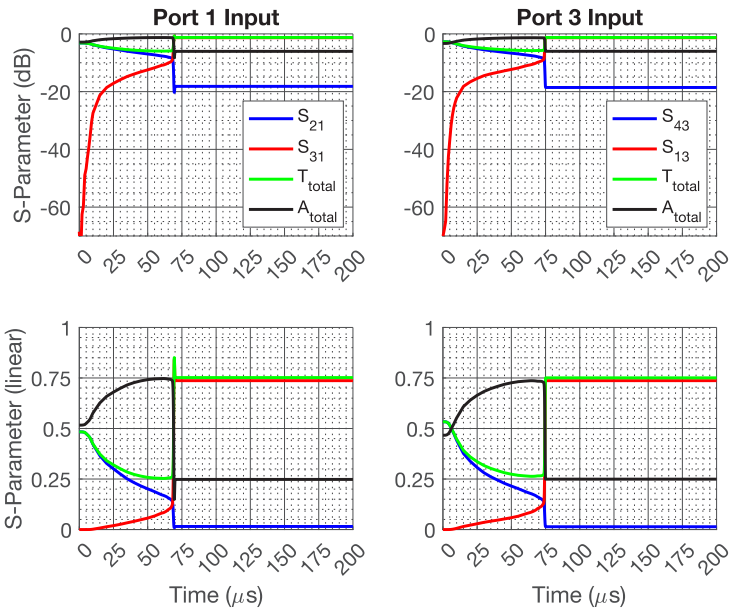

Fig. 9. Port transmittance behavior of the router through the MIT switching at VO_2 deactivation threshold (2.2 mW) for port 1 input case (68.9 µs) and port 3 input case (74.5 µs).

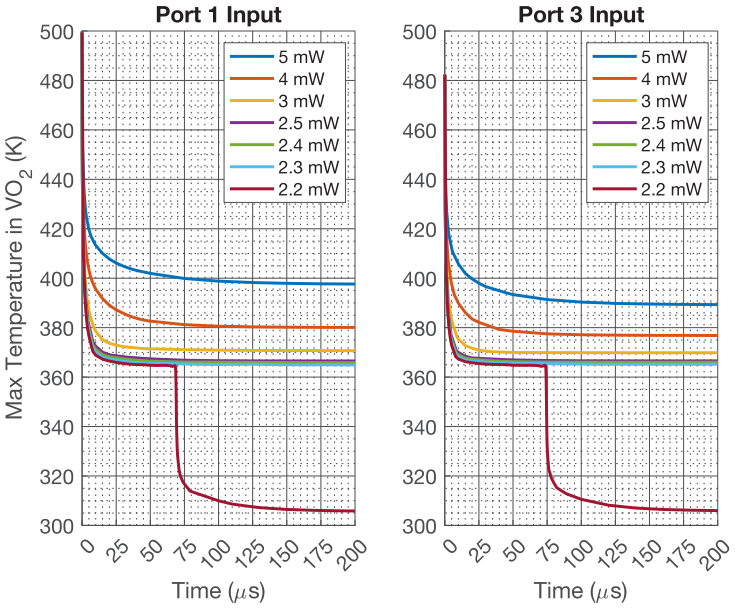

Fig. 10. Maximum temperature in VO_2 volume over the course of 200 µs to steady state, decreasing input power approaching and including deactivation.

Optics EXPRESS

4. Conclusion

We have demonstrated the phenomenon of asymmetric activation of phase change material VO_2 using a simulated mid-infrared optical router, bringing PCM-based asymmetry into the planar lightwave circuit domain. Using equal input power at opposite waveguide ports, we observe different heating behavior in the VO_2 material with the maximum steady state temperature increasing by 5.66°C/mW when applied in the port 1 input case and 5.74°C/mW when applied in the port 3 input case. These values are taken below the respective IMT activation thresholds of 7.1 mW and 7.2 mW. Additionally, the heat being concentrated in different areas of the device per input direction, there is more heat-sinking material to draw heat way when port 3 is used as the input. This results in lower steady state temperatures in the port 3 input case after VO_2's IMT and differing transient heating behavior than in the port 1 input case.

When cooling past the MIT deactivation threshold, both directions of input power allow the VO_2 to revert to its initial state at 2.2 mW but with the forward input deactivating sooner than the reverse by 5.6 µs. In addition to these asymmetries, the router exhibits performance metrics in the forward direction through the heating IMT of 56.5 dB power limiting and 48% rerouted power to port 2, and in the reverse direction through the heating IMT of 64.5 dB power limiting and 53% rerouted power to the port 4. For each input direction, initial total transmission is 75% with total absorptance 25%; this confirms the simulation's adherence to energy conservation. The total power lost before reaching the output port is the same in each case, but the proportion lost to heat in the VO_2 and to bending/radiation depends on input port.

As for bi-stability, the router maintains consistent routing performance with input powers down to 5 mW, after IMT takes place. This is a 30% reduction in input power from the activation threshold in the port 1 input case and a 31% reduction of the same in the port 3 input case. Input power of 4 mW yields only slight decreases from 48% to 46% in rerouted power for port 1 input and 53% to 49% for port 3 input. With the MIT deactivation power being 2.2 mW, the full bi-stability of the metallic state of VO_2 is described as a 69% reduction in input power from the IMT activation threshold. Thus, the quasi-latching behavior of the VO_2 device is proven. In the future, similar design schemes can be optimized to enhance this heating asymmetry effect to the advantage of strategic routing and power limiting capabilities, and other on-chip optical devices.

Funding. Air Force Office of Scientific Research (21RYCOR019); Air Force Research Laboratory (RY6-OSU-19-2-AFRL2); National Science Foundation (CAREER Award 1845370, 2149886).

Acknowledgments. Air Force Research Laboratory funding is in conjunction with Defense Associated Graduate Student Innovators (DAGSI).

Disclosures. The authors declare no conflicts of interest.

Data availability. Data underlying the results presented in this paper are not publicly available at this time but may be obtained from the authors upon reasonable request.

References

1. C. Wan, E. H. Horak, J. King, J. Salman, Z. Zhang, Y. Zhou, P. Roney, B. Gundlach, S. Ramanathan, R. H. Goldsmith, and M. A. Kats, "Limiting Optical Diodes Enabled by the Phase Transition of Vanadium Dioxide," ACS Photonics **5**(7), 2688–2692 (2018).
2. R. Thomas, E. Makri, T. Kottos, B. Shapiro, and I. Vitebskiy, "Unidirectional photonic circuit with a phase-change Fano resonator," Phys. Rev. A **98**(5), 053806 (2018).
3. R. Yahiaoui, J. Mathews, J. A. Burrow, I. Agha, G. Sevison, A. M. Urbas, A. Sarangan, and T. A. Searles, "Thermally Tunable Far-Infrared Metasurfaces Enabled by Ge2Sb2Te5 Phase-Change Material," in *Research and Applications of Photonics In Defense Conference* (IEEE, 2018), pp. 1–4.
4. A. Sarangan, J. Duran, V. Vasilyev, N. Limberopoulos, I. Vitebskiy, and I. Anisimov, "Broadband Reflective Optical Limiter Using GST Phase Change Material," IEEE Photonics J. **10**(2), 1–9 (2018).
5. R. Kononchuk, N. Limberopoulos, I. Anisimov, I. Vitebskiy, and A. Chabanov, "Photonic limiters with enhanced dynamic range," in *SPIE LASE* (SPIE, 2018), p. 7.
6. N. Antonellis, R. Thomas, M. A. Kats, I. Vitebskiy, and T. Kottos, "Nonreciprocity in Photonic Structures with Phase-Change Components," Phys. Rev. Appl. **11**(2), 024046 (2019).

Optics EXPRESS

7. A. Sarangan, "Design of resonant cavity thin film structures with complex active layers," J. Opt. Soc. Am. B **37**(11), 3461–3468 (2020).
8. M. Lust, S. Chen, C. E. Wilson, J. Argo, V. Doan-Nguyen, and N. Ghalichechian, "High-contrast, highly textured VO2 thin films integrated on silicon substrates using annealed Al2O3 buffer layers," J. Appl. Phys. **127**(20), 205303 (2020).
9. S. Chen, M. Lust, and N. Ghalichechian, "Antenna-coupled microbolometer based on VO2's non-linear properties across the metal–insulator transition region," Appl. Phys. Lett. **121**(20), 201901 (2022).
10. A. Shadmani, M. Miri, and S. Mohammadi Pouyan, "Ultra-wideband multi-level optical modulation in a Ge2Sb2Te5-based waveguide with low power consumption and small footprint," Opt. Commun. **439**, 53–60 (2019).
11. K. A. Hallman, K. J. Miller, A. Baydin, S. M. Weiss, and R. F. Haglund, "Sub-Picosecond Response Time of a Hybrid VO2:Silicon Waveguide at 1550 nm," Adv. Opt. Mater. **9**(4), 2001721 (2021).
12. N. A. Charipar, H. Kim, S. A. Mathews, and A. Piqué, "Broadband terahertz generation using the semiconductor-metal transition in VO2," AIP Adv. **6**(1), 015113 (2016).
13. S. Chen, M. Lust, A. Roo, and N. Ghalichechian, "Reliability of VO 2 -based mmWave Switches Under 100 Million Thermal Cycles," IEEE Trans. Device Mater. Reliab. **23**(2), 241–248 (2023).
14. B. J. Mapleback, K. J. Nicholson, M. Taha, T. C. Baum, and K. Ghorbani, "Complex Permittivity and Permeability of Vanadium Dioxide at Microwave Frequencies," IEEE Trans. Microwave Theory Tech. **67**(7), 2805–2811 (2019).
15. A. Mansingh, R. Singh, and M. Sayer, "Dielectric behaviour of vanadium dioxide," Phys. Stat. Sol. (a) **49**, 773–779 (1978).
16. C. Wan, Z. Zhang, D. Woolf, C. M. Hessel, J. Rensberg, J. M. Hensley, Y. Xiao, A. Shahsafi, J. Salman, S. Richter, Y. Sun, M. M. Qazilbash, R. Schmidt-Grund, C. Ronning, S. Ramanathan, and M. A. Kats, "Optical properties of thin-film vanadium dioxide from the visible to the far infrared," Ann. Phys. **531**(10), 1900188 (2019).
17. C. Zhang, C. Koughia, O. Güneş, J. Luo, N. Hossain, Y. Li, X. Cui, S.-J. Wen, R. Wong, Q. Yang, and S. Kasap, "Synthesis, structure and optical properties of high-quality VO2 thin films grown on silicon, quartz and sapphire substrates by high temperature magnetron sputtering: Properties through the transition temperature," J. Alloys Compd. **848**, 156323 (2020).
18. M. Currie, M. A. Mastro, and V. D. Wheeler, "Characterizing the tunable refractive index of vanadium dioxide," Opt. Mater. Express **7**(5), 1697–1707 (2017).
19. L. L. Fan, Y. F. Wu, C. Si, G. Q. Pan, C. W. Zou, and Z. Y. Wu, "Synchrotron radiation study of VO2 crystal film epitaxial growth on sapphire substrate with intrinsic multi-domains," Appl. Phys. Lett. **102**(1), 011604 (2013).
20. G. Hamaoui, N. Horny, C. L. Gomez-Heredia, J. A. Ramirez-Rincon, J. Ordonez-Miranda, C. Champeaux, F. Dumas-Bouchiat, J. J. Alvarado-Gil, Y. Ezzahri, K. Joulain, and M. Chirtoc, "Thermophysical characterisation of VO 2 thin films hysteresis and its application in thermal rectification," Sci. Rep. **9**(1), 8728 (2019).
21. Y. X. Guo, Y. F. Liu, C. W. Zou, Z. M. Qi, Y. Y. Wang, Y. Q. Xu, X. L. Wang, F. Zhang, and R. Zhou, "Oxygen pressure induced structure, morphology and phase-transition for VO2/c-sapphire films by PLD," Appl. Phys. A **115**(4), 1245–1250 (2014).
22. A. Matsuda, Y. Nozawa, S. Kaneko, and M. Yoshimoto, "Solid-phase epitaxy and pressure-induced topotaxy of the VO2 and V2O3 thin films on sapphire using annealing under uniaxial compression," Appl. Surf. Sci. **480**, 956–961 (2019).
23. T. Yamin, S. Wissberg, H. Cohen, G. Cohen-Taguri, and A. Sharoni, "Ultrathin Films of VO2 on r-Cut Sapphire Achieved by Postdeposition Etching," ACS Appl. Mater. Interfaces **8**(23), 14863–14870 (2016).
24. T.-H. Yang, R. Aggarwal, A. Gupta, H. Zhou, R. J. Narayan, and J. Narayan, "Semiconductor-metal transition characteristics of VO2 thin films grown on c- and r-sapphire substrates," J. Appl. Phys. **107**(5), 053514 (2010).
25. Y. Zhao, J. Hwan Lee, Y. Zhu, M. Nazari, C. Chen, H. Wang, A. Bernussi, M. Holtz, and Z. Fan, "Structural, electrical, and terahertz transmission properties of VO2 thin films grown on c-, r-, and m-plane sapphire substrates," J. Appl. Phys. **111**(5), 053533 (2012).
26. H. Kizuka, T. Yagi, J. Jia, Y. Yamashita, S. Nakamura, N. Taketoshi, and Y. Shigesato, "Temperature dependence of thermal conductivity of VO2thin films across metal–insulator transition," Jpn. J. Appl. Phys. **54**(5), 053201 (2015).
27. C. K. B. Viswanath, Z. Yang, and S. Ramanathan, "Geometric confinement effects on the metal-insulator transition temperature and stress relaxation in VO2 thin films grown on silicon," J. Appl. Phys. **109**(6), 063512 (2011).
28. L. Sánchez, S. Lechago, and P. Sanchis, "Ultra-compact TE and TM pass polarizers based on vanadium dioxide on silicon," Opt. Lett. **40**(7), 1452–1455 (2015).
29. L. D. Sánchez, I. Olivares, J. Parra, M. Menghini, P. Homm, J.-P. Locquet, and P. Sanchis, "Experimental demonstration of a tunable transverse electric pass polarizer based on hybrid VO2/silicon technology," Opt. Lett. **43**(15), 3650–3653 (2018).
30. H.-C. Ho, Y.-C. Lai, K. Chen, T. D. Dao, C.-H. Hsueh, and T. Nagao, "High quality thermochromic VO2 films prepared by magnetron sputtering using V2O5 target with in situ annealing," Appl. Surf. Sci. **495**, 143436 (2019).
31. S. Chen, M. Lust, and N. Ghalichechian, "Multiphysics simulation of hypersensitive microbolometer sensor using vanadium dioxide and air suspension for millimeter wave imaging," Microsyst. Technol. **27**(7), 2815–2822 (2021).